ISSN 0965-545X, Polymer Science, Series A, 2017, Vol. 59, No. 3, pp. 425–436. © Pleiades Publishing, Ltd., 2017.

COMPOSITES

Effect of Ceria and Zirconia Nanoparticles on Mechanical Behavior of Nanocomposite Hybrid Coatings[1]

Amir Ershad-Langroudi[a,*], Davoud Zare[a], and Azam Rahimi[b]

[a] *Colour and Surface Coatings Group, Polymer Processing Department, Iran Polymer and Petrochemical Institute (IPPI), Tehran, 14965/115 Iran*

[b] *Polymer Science Group, Polymer Science Department, Iran Polymer and Petrochemical Institute (IPPI), Tehran, 14965/115 Iran*

**e-mail: A.Ershad@ippi.ac.ir*

Received July 20, 2016;
Revised Manuscript Received November 3, 2016

Abstract—Epoxy-silica based hybrid nanocomposite coatings have been developed with different organic-inorganic contents by sol–gel process. Various ratios of ceria and zirconia colloidal dispersions as inorganic nanoparticles are uniformly distributed in the hybrid sol. The hybrid sols are prepared by hydrolysis and condensation of 3-glycidoxypropyltrimethoxysilane (GPTMS) and tetraethylorthosilicate (TEOS) in acidic solution using bisphenol A (BPA) and 1-methyl-imidazol (MI). A thin layer of each sol is coated on a micro-glass slide and 1050 aluminum alloy as substrates. The effect of alkoxysilane precursors (i.e. TEOS and GPTMS) and inorganic to organic molar ratio are investigated. Nanoindentation and dynamic mechanical analysis (DMA) performed to characterize the mechanical properties of the coatings in nanorange scale. It is revealed that all hybrid nanocomposite coatings had appropriate flexibility and strong interfacial interaction with the aluminum alloy substrate. It is proposed that the ceria and zirconia nanoparticles can be bonded to the surrounding of siloxane ring which can be induced high restriction in polymeric chain mobility in dynamic mechanical analysis. Nanoindentation tests showed that by increasing the inorganic phase in the nanocomposite, both elastic modulus and hardness increase, especially they are very intense in the higher levels of inorganic content.

DOI: 10.1134/S0965545X1703004X

INTRODUCTION

Aluminum and its alloys are among the most-used metals in the world [1]. The natural oxide layer can be formed on the surface of aluminum alloy in the atmosphere. However, this oxide layer is not able to protect the underlaying metallic substrate from corrosion in aggressive media [2]. In addition, the mechanical properties of natural oxide layer cannot resist against an abrasion or scratch condition. Therefore, any defects can be created on the coating, and the metal surface is exposed to an aggressive media, the metallic substrate will immediately start to corrode with serious effects on the adhesion of the coating and the integrity of the coated object. Such mechanical defects can not only occur when a product is used in service but also already during its production, for example, during forming processes of coated metallic sheets.

Therefore, a wide range of protection methods are developed to prolong lifetime or delay corrosion damages in metallic objects such as alloying, passivation, cathodic protection, sacrificial coatings, barrier coatings and corrosion inhibitors [3]. The addition of inorganic nanoparticles to the coating system is an established approach to improve the corrosion protection and mechanical resistance. The application of organic-inorganic nanocomposite coatings not only inhibits corrosive species from reaching the metal surface but also improves processability, scratch and abrasion resistant. In this regards, organic-inorganic hybrid nanocomposite coatings can provide outstanding corrosion protection and also mechanical resistance.

Nano inorganic particles such as SiO_2, TiO_2 and ZrO_2 in thermoset resins, have improved scratch and abrasion resistance of the coatings significantly [4, 5], without an important side effect on the transparency [6]. However, a key factor in the coating properties is a good dispersion of inorganic nanoparticles in the polymeric matrix [7].

The inorganic particles can be used in sol–gel process by silane coupling agents due to their bi-functional structure which can be reduced inorganic nanoparticles agglomeration by grafting organic groups on them. The results are an improvement in the

[1] The article is published in the original.

dispersion of inorganic particles because of the steric repulsion of grafted organic groups, and also an improvement in scratch and abrasion resistance of coatings [8–11].

The mechanical properties of hybrid thin coatings are of interest from both technologically and basic standpoints [12]. Nanoindentation is one of the prominent techniques to characterize the mechanical properties of hybrid thin layers in the nanometer range [13, 14]. Nanoindentation test has been routinely used to investigate the elastic–plastic and fracture properties of thin films [15, 16]. Methods for measuring the Young's modulus have been very well established for time independent materials [17]. Oliver and Pharr [18] proposed a method to determine the basic material properties such as Young's modulus. The method is based on Sneddon's solution [19] for the relationship between the load and displacement for an axisymmetric indenter indenting into a half-space composed of a linear elastic, isotropic and homogeneous material. While the method works well for time-independent materials, applying the methods directly to viscoelastic materials has experienced problems. For example, the unloading curve in viscoelastic materials sometimes has a negative slope, under situations where a small unloading rate and a relatively high load were used for a material with pronounced viscoelastic effects. Some work in recent years has improved the methods proposed by Oliver and Pharr [15, 18] for the determination of Young's modulus, or Young's relaxation modulus. Cheng et al. [20] investigated elastic and viscoelastic deformation under flat-punch indentation and derived the analytical solutions for linear viscoelastic deformation. Lu et al. [21] proposed methods to measure the creep compliance of solid polymers using either the Berkovich indenter or the spherical indenter and they also proposed a new method to measure the viscoelastic functions in frequency domain using a spherical indenter [22]. Their methods are applicable to any materials in linear viscoelastic domain and are characterized by the generalized Kelvin's model.

The mechanical behavior of coatings can be also investigated by nanoindentation test at different loading forces. Many important mechanical properties, such as hardness and elastic modulus can be obtained from the load—displacement data [23]. In addition, the fracture toughness of thin coatings can be calculated [24, 25]. Nanoscratch and wear tests can be also measured with a tangential force at ramping loads [26]. Recently, many efforts have been done to improve the properties of nanocomposite coatings with unique properties of inorganic compounds such as hardness and scratch resistance which also possess the good mechanical properties of organic polymers such as deformability and toughness [27]. Shokrieh et al. [28] investigated the effect of graphane nanoplatelets on the mechanical and tribological properties of epoxy based vinyl ester nanocomposite. The effect of titanium-based nanoparticle was studied on the mechanical properties of nanocomposite coating by nanoindentation methods [29]. Allahverdi et al. [30] investigated the effect of nanosilica on mechanical and thermal properties of epoxy resin. They found the elastic modulus and hardness improve by nanosilica content in the coating composition. Zhai and McKenna were performing a test sequence that includes multiple loading rates or indentation rates to extract polymer's viscoelastic properties [31].

3-glycidoxypropyltrimethoxysilane (GPTMS) could be used as a network former because of its dual functionality as well as a coupling agent in organic–inorganic hybrid systems. The results are a better dispersion of inorganic nanoparticles in organic matrix and an improvement in the mechanical properties of coating as well as a better adhesion to substrates. In the case of sol–gel-derived GPTMS–TEOS or tetramethoxyorthosilicate (TMOS) hybrid materials, it is found that organic content and hydrolysis water ratio have a significant effect on the corrosion resistance of hybrid coatings [32, 33]. Epoxy ring opening of GPTMS in sol–gel derived organic–inorganic materials with titanium and aluminum alkoxides [34], zirconium and cerium oxides [6] have been already investigated in our laboratory for corrosion protection of aluminum alloys.

In this research, epoxy-silica based hybrid nanocomposite coatings are prepared in the presence of CeO_2 and ZrO_2 water based colloidal nanoparticles by environmentally friendly sol–gel process. We have recently investigated the corrosion protection, glass transition temperature (T_g) and morphological properties of these nanocomposite coatings [6]. This work is in continuous of our previous study. Here, the mechanical properties of the nanocomposite coatings on 1050 aluminum alloy were studied in nanoscale. The aim of this work is to evaluate the influence of ceria and zirconia colloidal nanoparticles on the mechanical properties of the coating in this range. In each nanoindentation test, a loading history was prescribed to a coating layer and the resulting response was recorded, subsequently the experimental load–displacement curve was analyzed to determine the viscoelastic properties as a function of time.

EXPERIMENTAL

Materials and Reagents

Nanocomposite hybrid coatings were prepared using sol–gel precursors. Tetraethylorthosilicate (TEOS), was used as the inorganic network former and 3-glycidoxypropyl-trimethoxysilane (GPTMS), was used as the network modifier and coupling agent, supplied by Merck and Fluka, respectively. Both precursors were used as received. In addition, CeO_2 and ZrO_2 in aqueous colloidal dispersions were used as inorganic particles from Alfa Aesar. Bisphenol A

Table 1. Some characteristic data of the used materials

Material	Linear chemical formula	Description	Form
Tetraethylorthosilicate (TEOS)	$(C_2H_5O)_4Si$	Inorganic network former	Liquid
3-Glycidoxypropyl-trimethoxysilane (GPTMS)	$C_9H_{20}O_5Si$	Trifunctional silane epoxy ring monomer network modifier	Liquid
Cerium oxide	CeO_2	Inorganic nanofiller, low pH, <5.0 nm	Liquid, 20% in H_2O nanoparticle dispersion
Zirconium oxide	ZrO_2	Inorganic nanofiller, 5–10 nm particles in liquid	Liquid, 20% in H_2O nanoparticle dispersion
1-Methylimidazol (MI)	$C_4H_6N_2$	Catalyst for curing reaction	Liquid
Bisphenol A (BPA) Or Synonym 2,2-Bis(4-hydroxy phenyl) propane	$(CH_3)_2C(C_6H_4OH)_2$	Curing agent	Solid

(BPA) as curing agent, 1-methylimidazol (MI) used as catalyst for curing reaction, Sodium chloride and hydrogen chloride were supplied from Merck company. All materials were used without further purification. Some information regarding the characteristic of the materials used in this study including sol–gel precursors, inorganic particles, curing agent, initiator and catalyst is given in Table 1.

Sol Preparation

Firstly, GPTMS and TEOS are mixed in a beaker with 0.01 M HCl and ethanol in 1 : 2 H_2O/ethanol molar ratios at ambient temperature. Water to alkoxides is considered in the range of stoichiometric molar ratio. Then, a transparent sol was obtained by stirring two-phase solution at a rate of 240 rpm for 3 h. Secondly, ZrO_2 and CeO_2 colloidal nanoparticles dispersion in water were added to the sol while stirred during 30 min. Then, 1 : 1 molar ratio of bisphenol A (BPA) to epoxy silane was dissolved in the stirring sol. It was allowed the hydrolysis and polycondensation reactions in the sol by stirring at a rate of 240 rpm for 4 h at room temperature. In the following, 1-methylimidazol (MI) was added in the stirring sol as a cross-linking network catalysis (1 wt.% vs. GPTMS). Finally, the hybrid sol was coated on the 1050 AA and glass substrates after 5 min stirring. Table 2 shows the molar ratio of components in the prepared nanocomposite samples.

Substrate Preparation

The 1050 aluminum alloy and soda lime glass slides were used as substrates in this study. 1050 AA was polished by abrasive papers (number 400 and 600) to remove any oxide layer on the surface. The substrate was initially rinsed with Deionized water (DI H_2O), cleaned with ethanol to remove any excess dirt and other pollution. The etching solution was 5 wt % NaOH and the substrates were immersed into the solution for approximately 3 min at 60°C. Then, they were washed by deionized water to remove the etching solution remaining on the surface. After this step, the sample was immersed in a diluted HCl aqueous solution for 1 min at ambient temperature to desmutting. Finally, the substrate was rinsed with DI H_2O, cleaned with methanol/hexane to remove any excess probable pollution and dried before coating.

Coating

The hybrid sols were coated on the etched and cleaned substrates (i.e. 1050 AA and soda lime glass slides) through the spin-coating process with a spin rate of 1200 rpm, dried for 24 h at ambient temperature, and heated in oven for 2 h at about 130°C. The coating procedures may be repeated to obtain higher

Table 2. Prepared nanocomposite samples (in mol ratios[a])

Sample code	Organic phase[b], %	CeO_2/ZrO_2[c]	GPTMS/TEOS
GP1	100	0 : 0	1 : 0
GP2	66.6	0 : 0	2 : 1
GP3	62.5	1 : 0	2 : 1
GP4	58.8	1 : 1	2 : 1
GP5	55.5	2 : 1	2 : 1
GP6	33.3	0 : 0	1 : 2
GP7	0	0 : 0	0 : 1

[a] All mol fraction are based on 1 mol of GPTMS.
[b] Organic content (%) = ((mol GPTMS)/(mol GPTMS + mol TEOS + (mol CeO_2 + ZrO_2 nanoparticles)/5)) × 100.
[c] CeO_2 and ZrO_2 are used as 20% nanoparticle dispersion.

thickness. The soda lime glass slide was used as substrate to produce a transparent thin coating.

Transmission Electron Microscopy (TEM) Analysis

The three dimensional morphology of nanoparticles in the coated substrates were characterized by a Transmission electron microscopy (TEM Phillips CM-120 The Netherlands).

Dynamic Mechanical Analysis (DMA)

Dynamic Mechanical Analysis (DMA) experiments were measured on the powdered samples using DMTA-PL instrument, Tritic 2000 England in single cantilever bending mode in the temperature range from 0 to 200°C and 1 Hz frequency with a heating rate of 3 grad/min under nitrogen atmosphere according to ASTM E1640-04. In this study, nanocomposite coatings were scrapped from the surface and prepared as fine powder. The powdered samples were filled in the special steel mold with width 7.45 mm, length 30 mm and thickness of 1.2 mm. The steel mold has an elastic modulus at about 10^{11} Pa in the whole range of the experimental range of temperature. Therefore, the viscoelastic properties of samples can be attributed to the powdered samples.

Nanoindentation Test

Nanoindentation experiments were performed by using a Hysitron Inc. USA TriboScope® Nanomechanical Test Instrument with 2D transducer, complete software and Berkovich diamond indenter was used for performing indentation tests on the coated samples on 1050 aluminum alloy substrates. The thickness of the coating samples was in the range of 10 ± 2 μm to obtain intrinsic coating properties and to avoid the substrate effect.

For each sample, the five indents were performed at different points on the sample's surface according to the procedure described in ISO 14577 and the average values were reported in this study [35]. The normal load (P) was 300 μN with constant rate of 10 μN/s. The maximum load was kept constant for 10 s in order to minimize the viscoelastic behavior of the coating during the unloading segment i.e. creep or relaxation behavior. In the unloading step, the indenter tip was withdrawn from the sample surface at the same rate. Prior to nanoindentation tests, the calibration of Berkovich indenter area function was performed by using Oliver and Pharr methods [18] and a standard fused quartz sample. Figure 1 shows a typical loading—unloading nanoindentation curve as a function of displacement of indenter head [21, 36]. In Fig. 1, h_{max} indicates the displacement of indenter in the sample at the maximum load P_{max}, h_c and h_f are the depth of the indenter in contact with the sample under load and after complete unloading, respectively. ε is a constant with a value of 0.75 for a Berkovich indenter and depends on the geometry of indenter [18, 36].

Hardness and elastic modulus can be calculated from the indentation data, according to Oliver and Pharr method by Eq. (1) [18]. Thus, the hardness H could be measured from the maximum applied load P_{max}; divided by the projected contact area A at the maximum load:

$$H = \frac{P_{max}}{A}. \quad (1)$$

In this method, S is the initial unloading contact stiffness and is defined as a slop of unloading curve at the maximum load on load-displacement curve (see Fig. 1) [18]. The standard formulas for the evaluation of hardness and elasticity are given based on the assumptions according to the contact geometry sketched in Fig. 1 [18, 37].

RESULTS AND DISCUSSION

Hybrid Formation

3-glycidoxypropyltrimethoxysilane (GPTMS) as organically modified precursors with epoxy functional groups can react by hydrolysis and condensation via sol–gel processing with bisphenol A (BPA) and in the meantime condense with Tetraethoxy silane (TEOS) as inorganic precursors to produce organic–inorganic hybrid nanocomposite coatings. By the sol–gel process, two organic–inorganic incompatible phases are connected together with strong covalent bonds. The compatibility of two phases in nanocomposite network induces an improvement in optical transparency and mechanical properties of coating.

The organic–inorganic hybrid coatings have been performed in two steps. In the first step, GPTMS and TEOS are mixed with water and ethanol. In-situ silica nanoparticles are prepared with silanol from hydrolyzed GPTMS and/or TEOS. Accordingly, three principal sol–gel processing may occur as the formation of oxide network by hydrolysis and condensation reactions of TEOS and GPTMS in water and co-solvent (ethanol) media at low temperature by synthesis route shown in Scheme 2 in [6]. Therefore, the attachment of GPTMS and TEOS from their alkoxy side to each other is highly preferred and acts as a principal role in connecting organic and inorganic phases to each other. However, compatibility of organic and inorganic phases can be decreased by increasing TEOS content (i.e. in sample GP6). By increasing TEOS to GPTMS molar ratio in the sol composition, inorganic phase and the formation of Si–O–Si bond tend to increase which can be induced the larger inorganic entanglements in organic–organic network. The results may be representing a compact structure of hybrid network with an increasing trend for both of elastic modulus and hardness in hybrid coatings. For silicon compounds network connectivity is through

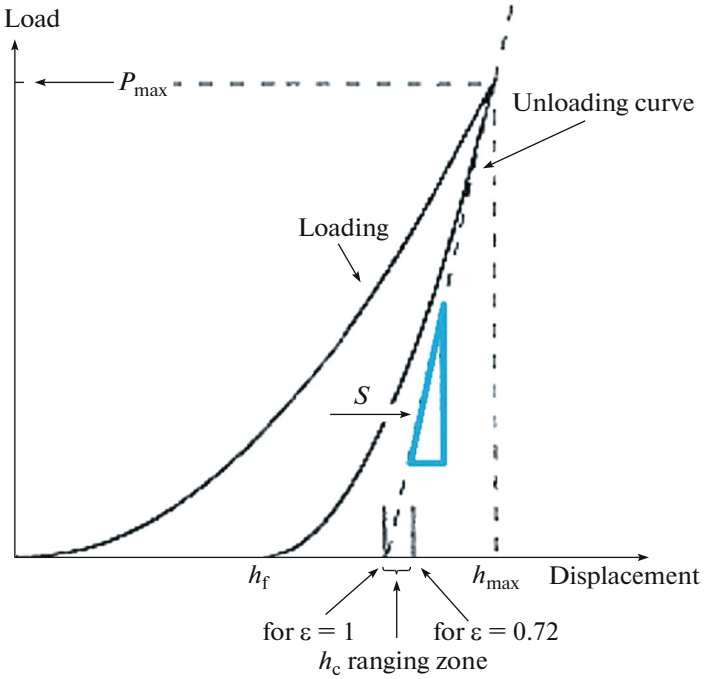

Fig. 1. (Color online) Schematic illustration of a typical loading—unloading nanoindentation curve.

the structural unit usually represented as Q^n, where Q represents Si as a central tetrahedral atom and n the number of bridging oxygen (BO) per Si tetrahedron that varies between 0 and 4 [38].

Structures of organically modified precursors (e.g. GPTMS) can be represented as Q^3 [39, 40]. Q^n units can also be used for identifying ring structures in the glass network. m-fold rings will be used for denoting cyclic silicates where m represents the number of Q^n units of silicon atoms in a ring [41].

For silica-based glasses obtained by sol–gel process, the desirable structure for cyclic silicates is 6-folded ring, which can be found in quartz and silica glass. Six-folded ring has bigger bridge angle and is less tensioned. It is thus kinetically more favorable.

GPTMS by 3 hydrolysable functional groups and long organic tail cannot form a complete ring structure and complete the glass network formation. At high GPTMS to TEOS molar ratio, the final hybrid coatings have less Q^3 units of silicon atoms in a ring structure.

Based on our previous research, we proposed a schema of reaction route for GPTMS and TEOS in the presence of CeO_2 and ZrO_2 nanoparticles based on 4-folded silicon atoms in an amorphous silica structure [6]. In addition, our TEM study on the sample G5 indicates a homogenously the ceria and zirconia nanoparticles incorporated in the coating structure (see Fig. 2).

Yahyaei et al. [42] also studied silica phase in UV curable acrylic resin by sol–gel process. Based on this study, they proposed a "defect structure" for inorganic network based on the vibration of 4-folded siloxane ring with the size of inorganic domain between 36 and 58 nm [43]. In our previous study, the average diameter of inorganic domains was reported 36.8 ± 1.6 and 53.6 ± 2.3 nm for GP4 and GP6 samples, respectively [6]. This may be indirectly implied a higher sili-

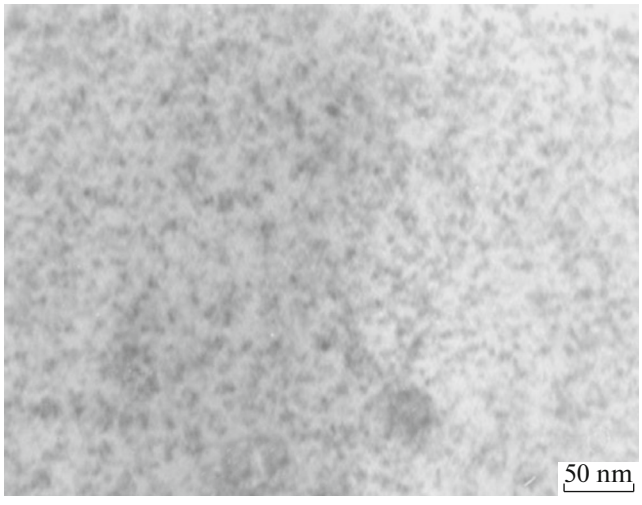

Fig. 2. TEM micrograph of coating prepared from GP5 hybrid sol.

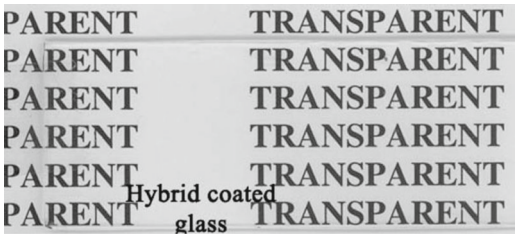

Fig. 3. Transparency of hybrid organic-inorganic nanocomposite coating (sample GP5).

oxane ring in the absence of ceria and zirconia nanoparticles.

In addition, sol–gel reaction provides opportunity for good dispersion of the aqueous ceria and zirconia colloidal nanoparticles with the silica sol in the presence of BPA as an organic component in water and co-solvent media at room temperature. In order to show the good transparency of the hybrid coatings, a coated glass slide sample was prepared from sol GP5 which was shown in Fig. 3. As overall result, the nanocomposite coating was completely transparent, continuous, and free of micro crack.

The ceria and zirconia nanoparticles can chemically bond to silanol groups in the sol through covalent bond formation. It is expected ceria and zirconia nanoparticles entered the siloxane ring and formed the core-shell morphology by silica inorganic network because of their particle sizes (i.e. 5–10 nm) [44]. However, Zr and Ce maps indicate their uniform distribution around some hollow spaces in the coating prepared from GP4 sample (see Figs. 7b–7d in [6]). This observation can be supported this idea that the ceria and zirconia nanoparticles are bonded to the surrounding of siloxane ring as schematic present in Fig. 4.

In addition, the bonding of ceria and zirconia nanoparticles to the outer siloxane ring can be induced high restriction in polymeric chain mobility. Real part of storage modulus (E') and tan δ curve versus temperature are presented in Figs. 5 and 6, respectively for sample GP5 containing ceria and zirconia nanoparticles in comparison with GP1 sample containing only inorganic silica structure. The results show the values of real storage modulus reduce slightly with the rise of temperature. However, the decreasing of storage modulus is more significant in the range of 50 to 80°C that can be attributed to passage of glass transition temperature region. It is observed that the storage modulus in both glassy and rubber region increased in the case of GP5 sample containing the silica structure and ceria and zirconia nanoparticles in compared with GP1 sample containing neat silica structure. The difference in real elastic modulus (E') for two nanocomposite samples, i.e. CP1 and GP5 at room temperature was about 10 percent while it increases to about 2 times in the passage of their glass transition temperatures. This can be an indication of the reinforcement effect of ceria and zirconia nanoparticles in both regions [45]. This higher modulus should be attributed to a "higher stiffening" induced by higher T_g [46].

As seen in Fig. 6, tan δ for both of nanocomposites shows a peak in this temperature range (50–80°C). In addition, with adding CeO_2 and ZrO_2 nanoparticles in the polymer network, the movement of polymer chain corresponding glass transition temperature (T_g), is more limited because these inorganic nanoparticles can decrease free volume and increase interaction in the polymer matrix and thus make the movement of

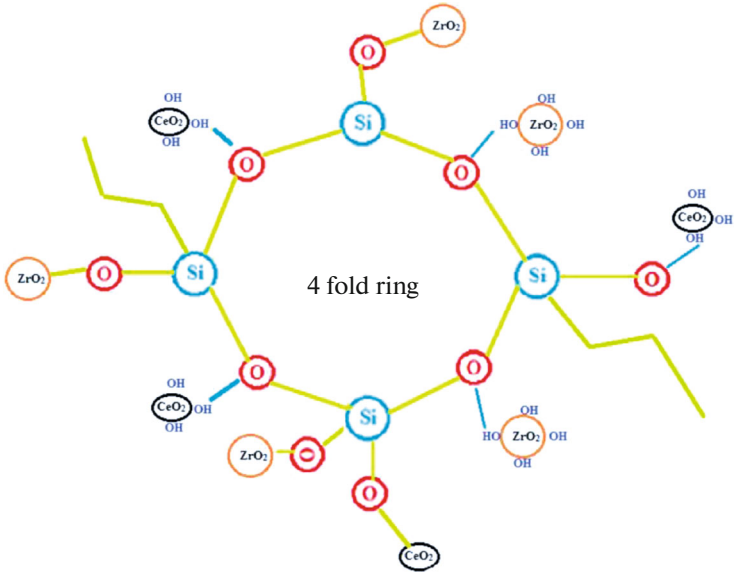

Fig. 4. (Color online) Schematic presentation of ceria and zirconia nanoparticles around silica ring structure.

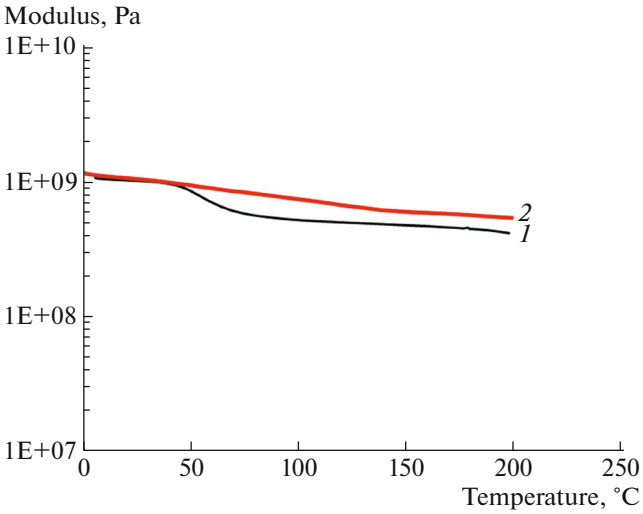

Fig. 5. (Color online) Real part of storage modulus (E') versus temperature for (*1*) GP1 and (*2*) GP5 hybrid nanocomposites samples at 1 Hz.

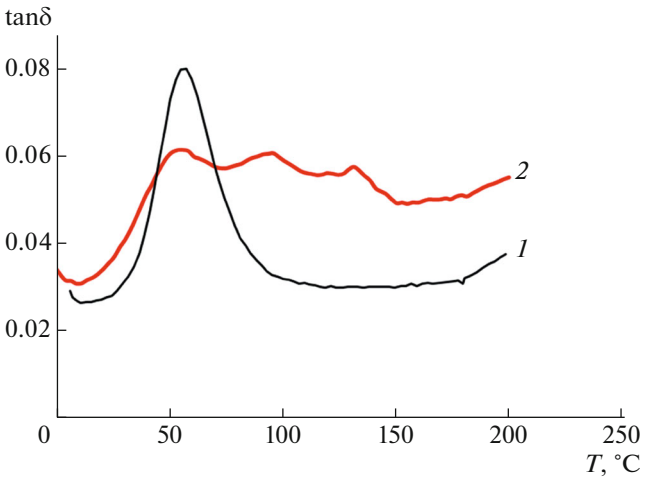

Fig. 6. (Color online) tan δ versus temperature for (*1*) GP1 and (*2*) GP5 hybrid nanocomposites samples at 1 Hz.

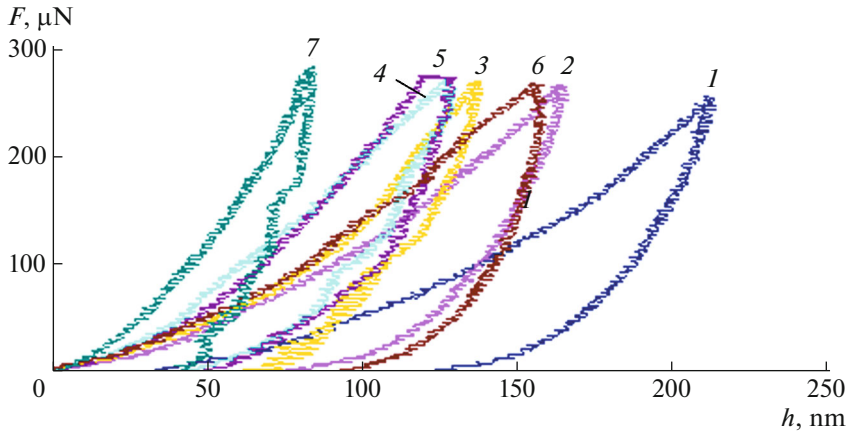

Fig. 7. (Color online) Load–displacement curves of nanoindentation experiments on nanocomposite coatings with various inorganic phases: (*1*) GP1, (*2*) GP2, (*3*) GP3, (*4*) GP4, (*5*) GP5, (*6*) GP6, and (*7*) GP7.

polymer chains more difficult which can be seen by an increasing in the glass transition temperature [47]. Furthermore, T_g is following by a wide and board peak in the rubber region as seen in tan δ for GP5 in compared with GP1 samples containing only inorganic silica structure. The similar results have already been reported for the sample GP4 [6]. In fact, the interfacial interaction between polymer chains and the nanoparticles can raise T_g. Therefore, it can be interpreted as the viscoelastic behavior of nanocomposite samples. In the temperature region close to T_g (50–80°C), the nanocomposite samples containing ceria and zirconia nanoparticles, i.e. GP5 here, behave like the neat polymer matrix, i.e. GP1, in colder temperature. This is perhaps the reason to observe a higher storage modulus and the limited rubbery state of the hybrid nanocomposite coatings.

Nanoindentation

In order to evaluate mechanical properties of nanocomposite coatings, nanoindentation test was performed on the GP1 to GP7 samples coated on 1050 AA substrate with various silica as well as CeO_2/ZrO_2 contents. Figure 7 displays load–displacement curves for nanocomposite coatings containing different inorganic phase ratios of nanoparticles. These curves were obtained from the nanoindentation test with a normal force of 300 μN.

By increasing inorganic content in the nanocomposite structure, nanoindentation curves shifted to the

left and the maximum penetration depth is reduced due to the increasing hardness.

By comparing the maximum penetration depth in the Load-displacement curves, it was determined a decreasing trend in h_{max} by increasing in the inorganic content in the nanocomposite structure. It may be attributed to the propagation of hard inorganic networking in the lattice structure which increases the penetration resistance of the material. As a result, the maximum depths indicate a decreasing trend while the maximum forces show an increasing trend. In addition, the unloading curve of the GP7 sample shows a noise. It may be related to the release of stress induced by unloading in a brittle silica inorganic network. Furthermore, the higher creep in GP5 sample at maintenance for 10 s at the maximum load may be attributed to the board domain with multiple relaxation peaks as seen in the Fig. 6.

The reduced elastic modulus and stiffness can be calculated from the top unloading curves by Eqs. (2) and (3):

$$E_r = \frac{\sqrt{\pi}S}{2\sqrt{A}}, \quad (2)$$

where S is the slope of the initial portion of the unloading curve and A is the indenter project area of contact [15, 18, 35, 48].

$$\frac{1}{E_r} = \frac{1-\vartheta_s^2}{E_s} + \frac{1-\vartheta_i^2}{E_i}, \quad (3)$$

where ϑ is the Poisson ratio and E is the elastic modulus, s and i subscripts related to sample and indenter properties, respectively. For diamond indenter E_i and ϑ_i are 1141 GPa and 0.07, respectively [18, 48, 49]. The value used for the Poisson's ratio of the nanocomposite coating is considered equal to 0.33.

As a practical matter, it is suggested that the unloading compliance and stiffness can be computed from a power relation fit of the unloading curve (see Eq. (4)) [18].

$$P = B(h - h_f)^m, \quad (4)$$

where B and m are fitting parameters and stiffness can be computed in the maximum penetration depth from Eq. (5) [23]:

$$S = \left(\frac{dP}{dh}\right)_{h=h_{max}} = Bm(h_{max} - h_f)^{m-1}. \quad (5)$$

The Berkovich tip used in practical nanoindentation testing is not an ideally sharp contact geometry type, therefore, tip geometry calibration or area function calibration is made on fused quartz by a series of indentation tests at depths of interest [23]. A plot of contact area A_c versus contact depth h_c can be curve fit according to a regression function (usually of power-law type) fitted to the unloading curve [23, 42]. Therefore, contact depth can be calculated from load-displacement from the Eq. (6).

$$h_c = h_{max} - \varepsilon\frac{P_{max}}{S}, \quad (6)$$

where ε is a constant and depends to the indenter geometry type. It is considered $\varepsilon = 0.75$ for Berkovich indenter tip. Figure 8 shows a column diagram for contact depth changes of different nanocomposite samples. As seen from statistical analysis of h_c in Fig. 8, the higher values for h_c are observed in GP1 and GP2 while GP7, GP4 and GP5 have the lower values, respectively. As the samples in this case are in the glassy region, such behavior should be attributed in their elastic properties. By adding inorganic phase, the elasticity of samples increase and the contact depth is reduced.

The maximum of stiffness values can be computed from the slope of the unloading curve in h_{max}. Figure 9a is shown the stiffness changes for the different nanocomposite samples. As clearly seen from this graph, the stiffness is following upward trend with increasing percentage of inorganic phase in the nanocomposite.

By obtained stiffness values and using Eq. (2), the reduced elastic modulus E_r is calculated and by using the Eq. (3), the elastic modulus of samples (E_s or E) are determined. Figure 9b is shown the elastic modulus for the different nanocomposite samples. The hardness values can be calculated from Eq. (1). Statistical analysis of elastic modulus and hardness data (see Fig. 9c) showed that by increasing the inorganic phase, they follows an increasing trend, especially it is more intense at higher levels of inorganic phase. This phenomenon can be explained as the elastic modulus can be significantly affected by adding hardener inorganic nano particles. However, hardness (H) may be partially related to the cross link density and the adhesion energy. As seen for the hardness, by adding nanoparticles to GPTMS and curing, crosslink density can be increased resulting in increasing hardness values. It is interesting to compare the indentation modulus with the modulus values that are obtained by using DMA experimental technique. Figure 5 shows that the storage moduli of GP5 is about 10% higher than its of GP1 at room temperature but it increases up to 2 fold in passage of T_g. Figure 9b indicates that indentation modulus of GP5 sample almost double that of GP1 sample. It is related to the difference in the type of modulus information that can be obtained with two techniques, i.e. DMA and nanoindentation. DMA experimental technique provides a bulk modulus for the whole sample depending on the amount of nanoparticles and their dispersions in the matrix, but nanoindentation test represents a local modulus related to a very small zone influenced by the nanoparticles. For this reason, nanoindentation shows

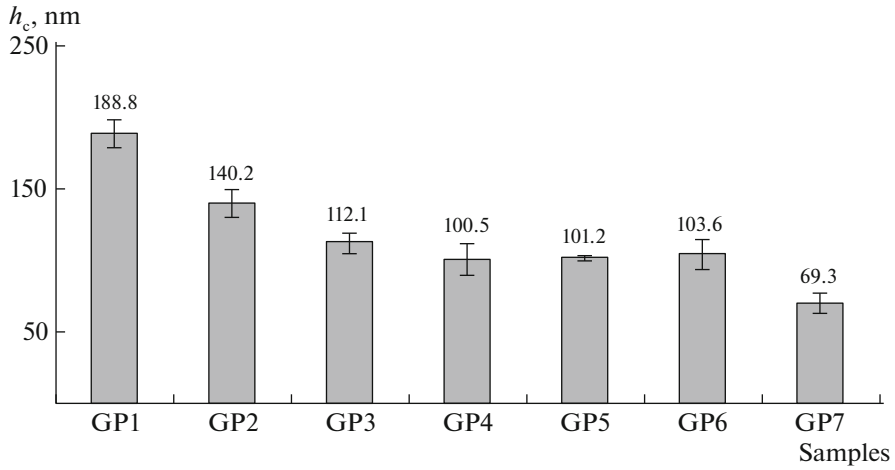

Fig. 8. Contact depth of nanocomposite coating.

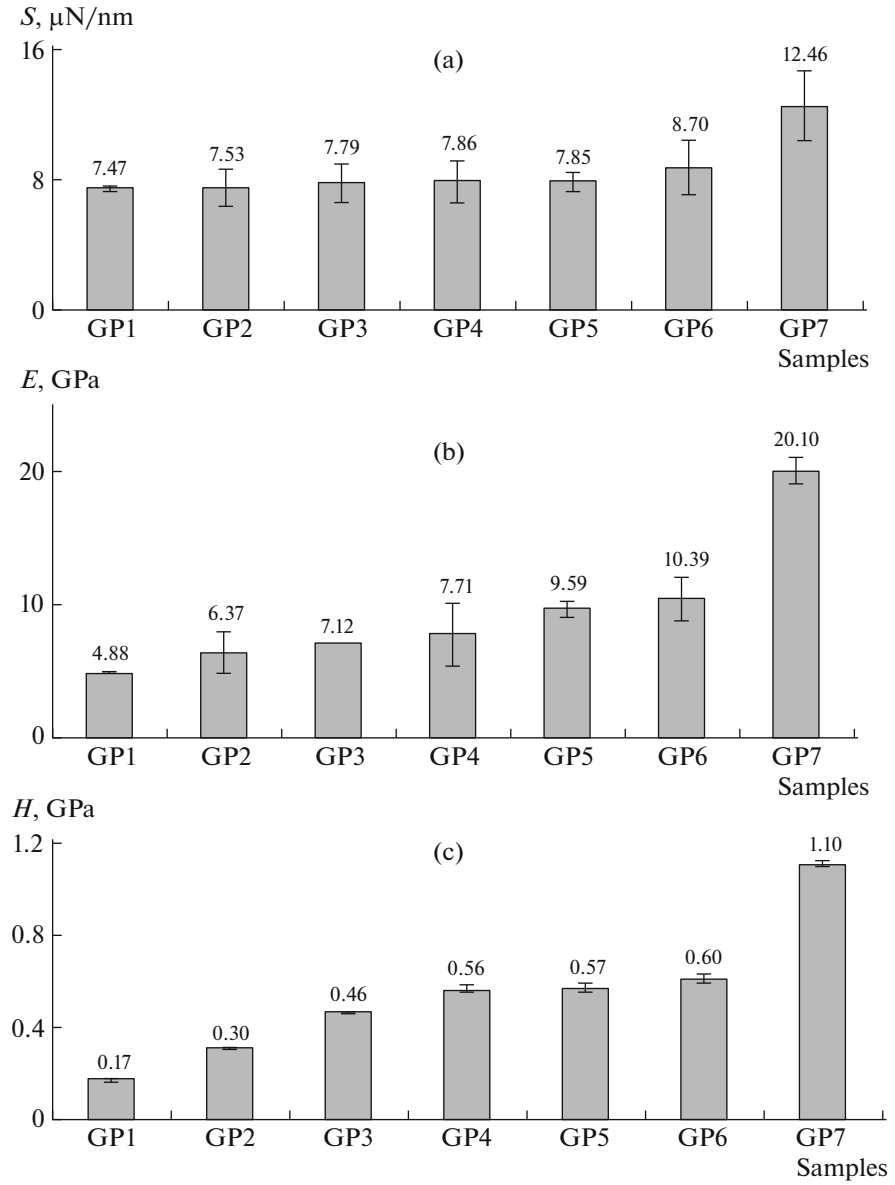

Fig. 9. (a) Stiffness, (b) elastic modulus, and (c) hardness for different nanocomposite samples (each sample 3–5 times).

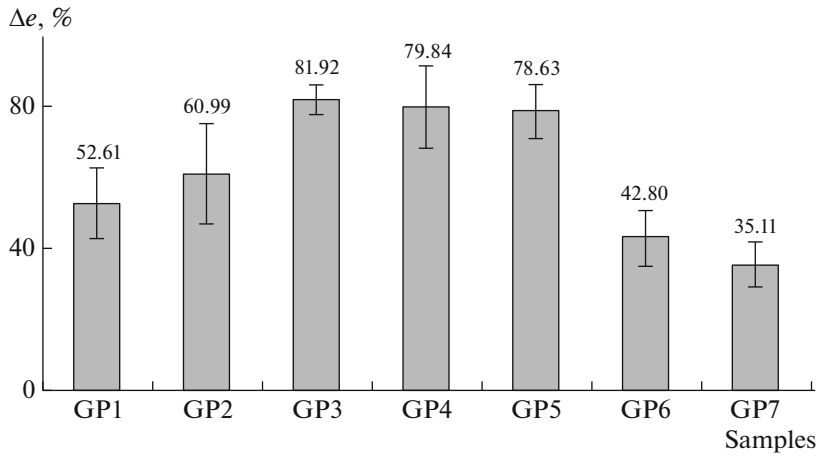

Fig. 10. Elastic Recovery Δe for different nanocomposite coatings.

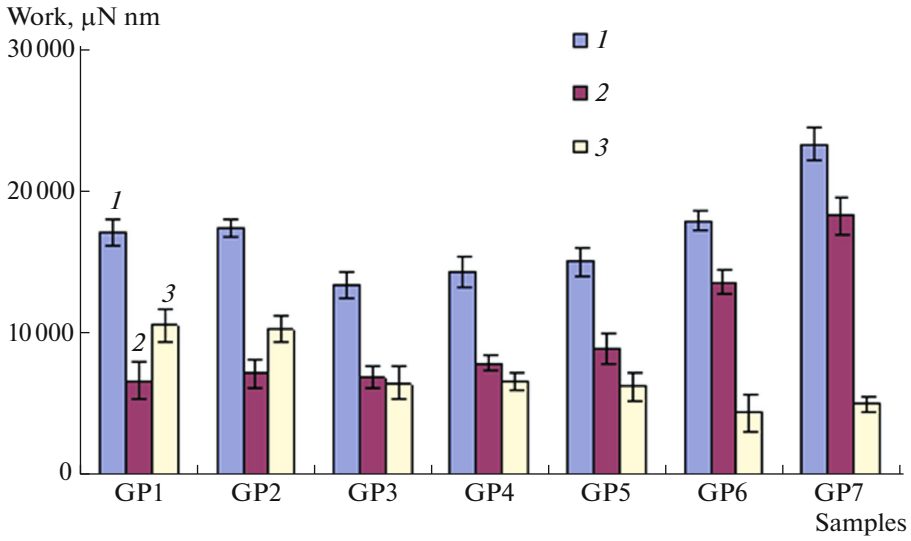

Fig. 11. (Color online) The bar chart of changes in (*1*) total work U_T, (*2*) elastic work U_E, and (*3*) plastic work U_P for the investigated nanocomposite samples.

a large stiffing modulus and DMA doesn't indicate much change at room temperature.

Another important parameter is the recovery elastic that is proportional with plastic deformation during the penetration process. The recovery elastic Δe can be obtained from loading-unloading curve, and defines as following equation:

$$\Delta e = \frac{h_{\max} - h_{\mathrm{f}}}{h_{\max}} \times 100\%, \quad (7)$$

where $h_{\max}$ is the maximum penetration depth and h_{f} is the residual plastic depth after completing unloading.

Figure 10 exhibits the graphical changes of elastic recovery samples. The elastic recovery samples show a maximum for the GP3 to GP5 samples containing ceria and zirconia nanoparticles. The results of two samples, GP6 and GP7, can be explained by high percentage of silica inorganic networking induce an elastic-brittle behavior of the samples. As seen in the unloading curve of GP7 in Fig. 7, the noise in unloading curve may be related to brittle behavior in the sample.

The total amount of work as well as elastic (viscoelastic) part and plastic part, can be calculated respectively based on the area under the load-displacement curve, unloading curve corresponding the elastic (viscoelastic) part, and the plastic part which is a difference between total work and elastic part (see Eqs. (8) and (9)).

$$U_T = \int F_N dh, \quad (8)$$

$$U_p = U_T - U_E. \quad (9)$$

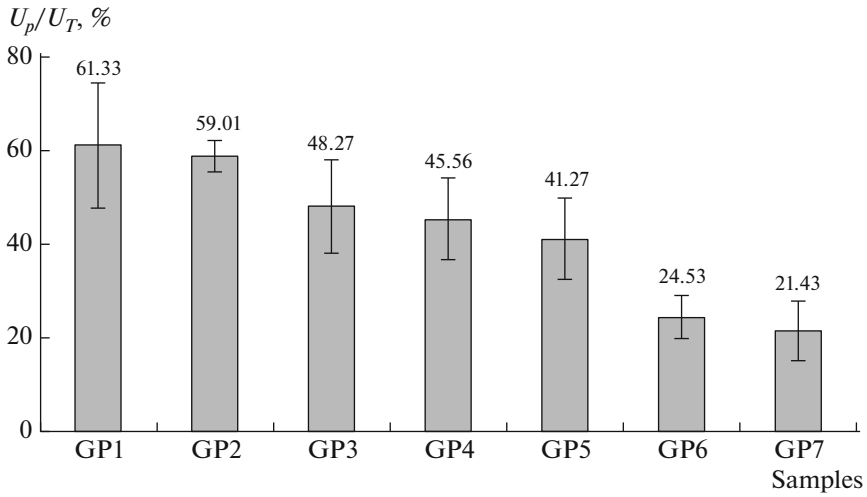

Fig. 12. The changes of plasticity index for different nanocomposite samples.

Figure 11 shows the bar chart of changes in total work (U_T), elastic work (U_E) and plastic work (U_P) for the prepared nanocomposite coatings. As seen in this figure, by increasing silica content in the nanocomposite composition, total work (U_T) and elastic work (U_E) follow up an increasing trend while plastic work (U_P) under goes an opposite trend. This may be indirectly implied a higher silioxane ring networking by increasing silica content in the samples that has high susceptibility of Si–O–Si bonds in the segment movements, and their high elasticity. However, increasing inorganic phase by adding ceria and zirconia nanoparticles does not provide important changes in trend of elastic work (U_E) and plastic work (U_P). This observation can be also supported the proposed idea that the ceria and zirconia nanoparticles are bonded to the outer surrounding of siloxane ring. Therefore, they are not expected to have a significant role in propagation of silica networking.

$$U, \% = (U_p/U_T) \times 100\%. \quad (10)$$

Furthermore, the plasticity index can be calculated by normalization of the plastic to total work according to Eq. (10).

As seen in Fig. 12, the plasticity indexes exhibit a decreasing trend by adding the inorganic phase for different nanocomposite samples. Reduction in plasticity indexes with increasing inorganic content in the nanocomposite samples can be an indication of recovery in reversible response of sample to applied load. In addition, comparison of GP3 to GP5 samples shows that the samples with different ZrO_2 and CeO_2 contents but constant TEOS/GPTMS ratio have similar plastic deformation. This also corresponds to a less inorganic networking structure in constant TEOS containing nanocomposite samples.

CONCLUSIONS

Nanocomposite coatings were prepared using silane precursors (i.e., TEOS and GPTMS), BPA, and CeO_2 and ZrO_2 colloidal nanoparticles by sol–gel process. According to the results, the ceria and zirconia nanoparticles homogenously incorporated in the silica based nanocomposites. The results support this idea that the ceria and zirconia nanoparticles can be bonded to the surrounding of siloxane ring by a core shell structure.

In addition, the coatings are uniform and transparent. Silica based nanocomposite coatings modified with CeO_2·and ZrO_2 nanoparticles can be used as fillers to improve the mechanical properties of 1050 aluminum alloy as well as its corrosion resistance in the previous electrochemical studies. DMA results indicated that real part of storage modulus (E') increased and the relaxation process corresponding to T_g value decreased and following by a wide and board peak with adding the ceria and zirconia nanoparticles in the nanocomposites composition. The elastic recovery results showed that among the prepared samples, the GP3 to GP5 had the higher values, owing to the presence of two distinct nanoparticles and the high portion of the organic phase.

REFERENCES

1. A. Lutz, O. V. D. Berg, J. V. Damme, K. Verheyen, E. Bauters, I. D. Graeve, F. E. D. Prez, and H. Terryn, ACS Appl. Mater. Interfaces **7**, 175 (2015).
2. U. Riaz, C. Nwaoha, and S. M. Ashraf, Prog. Org. Coat. **77**, 743 (2014).
3. D. Landolt, *Corrosion and Surface Chemistry of Metals* (CRC Press, Boca Raton, FL, 2007), pp. 513–584.
4. H. J. Glasel, F. Bauer, H. Ernst, M. Findeisen, E. Hartmann, and H. Langguth, Macromol. Chem. Phys. **201**, 2765 (2000).

5. S. Sepeur, N. Kunze, B. Werner, and H. Schmidt, Thin Solid Films **35**, 216 (1999).
6. A. Ershad-Langroudi and A. Rahimi, Iran. Polym. J. **23**, 267 (2014).
7. Y. Z. K. Lahijani, M. Mohseni, and S. Bastani, J. Coat. Technol. Res. **10**, 537 (2013).
8. S. Sun, C. Li, L. Zhang, H. L. Du, and J. S. Burnell-Gray, Eur. Polym. J. **42**, 1643 (2006).
9. M. Iijima, M. Tsukada, and H. Kamiya, J. Colloid Interface Sci. **307**, 418 (2007).
10. M. Rostami, M. Mohseni, and Z. Ranjbar, Pigm. Resin Technol. **40**, 363 (2011).
11. D. Işın, N. Kayaman-Apohan, and G. Güngör, Prog. Org. Coat. **65,** 477 (2009).
12. J. C. Tan and A. K. Cheetham, Chem. Soc. Rev. **40**, 1059 (2011).
13. D. Guo, G. Xie, and J. Luo, J. Phys. D: Appl. Phys. **47**, 013001 (2014).
14. C. Sanchez, C. Boissière, D. Grosso, C. Laberty, and L. Nicole, Chem. Mater. **2**, 682 (2008).
15. W. C. Oliver and G. M. Pharr, J. Mater. Res. **19**, 3 (2004).
16. J. L. Hay and G. M. Pharr, "Instrumented Indentation Testing," in *ASM Handbook, **Vol. 8**: Mechanical Testing and Evaluation*, Ed. by H. Kuhn and D. Medlin, 10th ed. (ASM International, Materials Park, OH, 2000), pp. 232–243.
17. Q. Kan, W. Yan, G. Kang, and Q. Sun, J. Mech. Phys. Solids **61**, 2015 (2013).
18. W. C. Oliver and G. M. Pharr, J. Mater. Res. **7**, 1564 (1992).
19. I. N. Sneddon, Int. J. Eng. Sci. **3**, 47 (1965).
20. L. Cheng, X. Xia, W. Yu, L. E. Scriven, and W. W. Gerberich, J. Polym. Sci., Part B: Polym. Phys. **38**, 10 (2000).
21. H. Lu, B. Wang, J. Ma, G. Huang, and H. Viswanathan, Mech. Time-Depend. Mater. **7**, 189 (2003).
22. G. Huang, B. Wang, and H. Lu, Mech. Time-Depend. Mater. **8**, 345 (2004).
23. X. Li and B. Bhushan, Mater. Charact. **48**, 11 (2002).
24. J. Chen, J. Phys. D: Appl. Phys. **45**, 203001 (2012).
25. C. McManamon, J. P. de Silva, J. Power, S. Ramirez-Garcia, M. A. Morris, and G. L. W. Cross, Langmuir **30**, 11412 (2014).
26. G. Rivero, L. A. Fasce, S. M. Ceré, and L. B. Manfredi, Prog. Org. Coat. **77**, 247 (2014).
27. X. Zhang, L. Hu, and D. Sun, Acta Mater. **54**, 5469 (2006).
28. M. M. Shokrieh, M. R. Hosseinkhani, M. R. Naimi-Jamal, and H. Tourani, Polym. Test. **32**, 45 (2013).
29. A. Tiwari and L. H. Hihara, Prog. Org. Coat. **77**, 1200 (2014).
30. A. Allahverdi, M. Ehsani, H. Janpour, and S. Ahmadi, Prog. Org. Coat. **75**, 543 (2012).
31. M. Zhai and G. B. McKenna, J. Polym. Sci., Part B: Polym. Phys. **52**, 633 (2014).
32. R. Zandi-zand, A. Ershad-langroudi, and A. Rahimi, Prog. Org. Coat. **53**, 286 (2005).
33. R. Zandi-zand, A. Ershad-langroudi, and A. Rahimi, J. Non-Cryst. Solids **351**, 1307 (2005).
34. H. Abdollahi, A. Ershad-Langroudi, A. Salimi, and A. Rahimi, Ind. Eng. Chem. Res. **53**, 10858 (2014).
35. *ISO 14577: Metallic Materials—Instrumented Indentation Test for Hardness and Materials Parameters—Part 1: Test Method, International Organization for Standardization,* 2002.
36. A. Ershad Langroudi, Int. J. Bio-Inorg. Hybrid. Nanomater. **2**, 337 (2013).
37. M. R. Naimi-Jamal and G. Kaupp, Z. Metallkd. **96**, 1226 (2005).
38. H. Aguiar, J. Serra, P. Gonzalez, and B. León, J. Non-Cryst. Solids **355**, 475 (2009).
39. C. Jäger, P. Hartmann, R. Witter, and M. Braun, J. Non-Cryst. Solids **263–264**, 61 (2000).
40. M. Magi, E. Lippmaa, A. Samoson, G. Engelhardt, and A. R. Grimmer, J. Phys. Chem. **88**, 1518 (1984).
41. J. Gonzalez-Hernández, J. F. Pérez-Robles, F. Ruiz, and J. R. Martínez, Superficies Vacio **11**, 1 (2000).
42. H. Yahyaei and M. Mohseni, Tribol. Int. **57**, 147 (2013).
43. H. Yahyaei, M. Mohseni, and S. Bastani, in *Proceeding of Seventh Coating Science International Conference, Noordwijk, Netherlands, 2011* (Noordwijk, Netherlands, 2011).
44. R. Kasemann and H. Schmidt, in *Proceeding of First European Workshop on Hybrid Organic–Inorganic Materials, Chateau de Bierville, France, 1993* (Chateau de Bierville, France, 1993), p. 171.
45. A. Allahverdi, M. Ehsani, H. Janpour, and S. Ahmadi, Prog. Org. Coat. **75**, 543 (2012).
46. X. Li and G. B. McKenna, ACS Macro Lett. **1** (3), 388 (2012).
47. R. Y. Kannan, H. J. Salacinski, P. E. Butler, and A. M. Seifalian, Acc. Chem. Res. **38**, 879 (2005).
48. L. Gan, J. Wang, and R. M. Pilliar, Biomaterials **26**, 189 (2005).
49. H. Bei, Y. F. Gao, S. Shim, E. P. George, and G. M. Pharr, Phys. Rev. B **77**, 060103 (2008).